DYNAMIC MODEL OF NICKEL HYDROGEN BATTERY – THE VIRTUAL TEST BED IMPLEMENTATION

Shengyi Liu [a], Roger A. Dougal [a], John W. Weidner [b], and Lijun Gao [a]
[a] Electrical Engineering Department
[b] Chemical Engineering Department
University of South Carolina
Columbia, SC 29208 USA
lius@engr.sc.edu

Abstract

A dynamic model of a nickel hydrogen battery implemented in the Virtual Test Bed (VTB) is presented. The battery system is simplified as such one-electron-transfer redox reaction of nickel hydroxide and nickel oxyhydroxide occurs uniformly and isothermally throughout the entire battery. The reversible potential includes the effect of multiphase activities of nickel oxyhydroxide. The overcharge process is characterized by the oxygen reaction. The thermal modeling includes reversible heat. The detailed model equations are derived for VTB implementation, and the characteristics of the battery are presented based on the VTB simulation and in good agreement with the experimental data.

Key Words

Dynamic model, nickel hydrogen battery, non-ideal reversible potential, overcharge, Virtual Test Bed.

I. Introduction

The nickel hydrogen battery (Ni-H_2) [1, 2] has been a strong contender as a major energy storage device in spacecraft power systems [3, 4, 5]. Therefore it is necessary to study its dynamic behaviors under different system configurations and environmental conditions, so that the knowledge of the battery's power capability, cycle life and operating reliability can be achieved for optimization of system designs. The approach to model the Ni-H_2 battery in the Virtual Test Bed (VTB) [6] starts with considering the battery as a system governed by physics laws under certain conditions (initial charge, ambient temperature, and load, etc.). Hence an interdisciplinary – thermal, electrical and chemical – system is involved. Given a time, the battery interacts with surroundings in two ways: it delivers (or absorbs) electrical power to the load at its electrical terminals, and it absorbs or releases heat to ambient through its surface. Thus, the dynamic behavior is a result of coupled electrochemical, chemical-thermal and electrothermal processes for given initial and boundary conditions. In our model, the solution to the coupled processes is obtained by means of Resistive-Companion (RC) method [7], in which the governing equations are time-discretized to a standard matrix formulation in terms of across and through variables and solved through the VTB simulation simultaneously. In the subsequent sections, we will discuss energy conversion processes in the battery, detailed VTB implementation, and simulation results.

II. Energy Conversion Processes

To construct a VTB model for the Ni-H_2 battery, we first discuss each of energy conversion processes, based on which the terminals for power transfer can be derived in RC format. Internally, the electrochemical process turns chemical energy into work in a form of electricity for a discharge event, or from electrical to chemical form for a charge event. In the meantime, thermal energy conversion processes occur associatively: entropic heat, polarization heat [8] and heat due to an isometric process of the gas phase. The charge transport in the battery experiences various overpotentials caused by surface kinetics, concentration limitation and ohmic loss. These can be categorized as electrothermal processes resulting in polarization heat or irreversible heat. Entropic heat, a result of entropy change, is reversible. Heat due to isometric process of the gas phase is reversible. In addition, thermal processes such as enthalpy of mixing, phase change, and change of specific heat also take place, affecting the overall thermal behavior of the battery. Externally, the battery delivers or receives electrical power through its electrical terminals and heat power through its thermal terminal.

A. Electrochemical Process

The electrochemical process is the base on which we derive the reversible potential of the battery. It is assumed that the charge and discharge processes are in such a controlled way that the rate of charge and discharge is near or less 0.5C to ensure a reliable, safe and long lifetime operation (e.g. in spacecraft power systems). Under the circumstances, the charge, mass and heat transfer, and the equilibrium state can be assumed to complete instantly, thus the kinetics of reactions is not a limiting factor to the external characteristics. This leads to the assumption that the electrochemical and electrothermal processes take place uniformly and isothermally throughout the battery. By assuming that, it

greatly simplifies the modeling process while observing the major features of the battery. Another important consideration for the reversible potential is its deviation from the ideal Nernst equation. The nonideality, due to ordered intercalation of multi-phase nickel oxyhydroxide [9], is included in the model. The phase reactions of nickel oxyhydroxide strongly affect the characteristics of the reversible potential, and having a positive effect on the battery capacity [10, 11]. The hydrogen reaction at the platinum electrode is trivial, resulting in a current equal to the nickel reaction current, and a constant potential that can be taken into account in the overall reversible potential. Now the characterization of the reversible potential of the battery can be proceeded as if a usual one-electron-transfer redox reaction occurs between nickel hydroxide and nickel oxyhydroxide.

To characterize the overcharge process, the current resulted from the oxygen reduction is considered. It was believed [10, 11] that the water oxidation/reduction (or oxygen evolution) at the nickel electrode and the oxygen reduction at the platinum electrode play a dominant role in an overcharge process. Part of the oxygen produced at the positive electrode diffuses to the platinum electrode and reduces there during an overcharge event, thereby causing a large portion of the current wasted for oxygen reduction. For normal charge and discharge, the oxygen reduction yields negligible current.

In summary, the electrochemical reactions that characterize the energy conversion between chemical and electrical forms in Ni-H_2 battery are given below.
At the nickel electrode are the nickel reduction/oxidation and the water reduction/oxidation:

$$N_iOOH + H_2O + e^- \underset{discharge}{\overset{charge}{\leftrightarrows}} N_i(OH)_2 + OH^- \tag{1}$$

$$\frac{1}{2}O_2 + H_2O + 2e^- \leftrightarrows 2OH^- \tag{2}$$

At the platinum electrode are the hydrogen reaction and the oxygen reduction:

$$\frac{1}{2}H_2 + OH^- \underset{discharge}{\overset{charge}{\leftrightarrows}} H_2O + e^- \tag{3}$$

$$\frac{1}{2}O_2 + H_2O + 2e^- \rightarrow 2OH^- \tag{4}$$

The overall reversible potential for the reactions (1) and (3) is given below.

$$E_{N_i}(T,x) = E^0_{N_i}(T) + \frac{RT}{F}\ln\left(\frac{1-x}{x}\right) + \frac{RT}{2F}\left[A_0(T)C(x) + B_0(T)D(x)\right] \tag{5}$$

where E_{N_i} (in volts) is the total reversible potential, R and F are the gas constant (8.314 J/mol/K) and Faraday constant (96,485 coulombs/mol) respectively. T and x are the absolute temperature (in kelvin) and the state of discharge of the battery, both are the functions of the independent variable time t. The third and last term in (5) are for the nonideality of the reversible potential. Notice that $E^0_{N_i}$, A_0 and B_0 are functions of temperature only, and C and D are functions of the state of discharge only. They are given by,

$$A_0(T) = a_0 + a_1 \cdot T \tag{6}$$

$$B_0(T) = b_0 + b_1 \cdot T \tag{7}$$

$$C(x) = c_0 + c_1 \cdot x \tag{8}$$

$$D(x) = d_0 + d_1 \cdot x + d_2 x^2 \tag{9}$$

$$E^0_{N_i}(T) = \begin{cases} e_{0d} + e_1 \cdot T, & for \quad discharge \\ e_{0c} + e_1 \cdot T, & for \quad charge \end{cases} \tag{10}$$

where a_i, b_i, c_i, and d_i are constants that specify phase activities of nickel oxyhydroxide, which may vary from one battery to another due to different contents and pore structures. e_{0c}, e_{0d} and e_1 are also constants. The difference between e_{0c} and e_{0d} for charge and discharge events in (10) is used to characterize the hysteresis of proton intercalation in nickel hydroxide electrode [12, 13].

The current of oxygen reaction can be calculated according to the Butler-Volmer equation,

$$i_{O_2}(v,T) = AL_+ ai_{0,O_2}(T)\exp\left[4(1-\alpha_{O_2})\frac{F}{RT}\left(v - E_{O_2}(T)\right)\right] \tag{11}$$

where i_{O_2} is the oxygen reaction current (amps). α_{O_2} (0.75) is the reaction transfer number, A and L_+ are the electrode area (m^2) and thickness (m) respectively, and v is the battery terminal voltage (volts). E_{O_2} is the reaction potential (volts), and it is given by equation (12). a is the specific area (m^2/m^3) of the electrode, and $i_{O_2,0}$ is the exchange current density (amps/m^2), for which we assume that it follows the Arrhenius equation. The product of a and $i_{O_2,0}$ is given by equation (13).

$$E_{O_2}(T) = 1.730 - 0.00168 \cdot T \tag{12}$$

$$ai_{O_2,0}(T) = 10.0\exp\left[-12{,}025\left(\frac{1}{T} - \frac{1}{298}\right)\right] \tag{13}$$

The state of discharge x, at any time t, is determined by the available nickel active material in the battery. It can be conveniently related to the nickel reaction current i_{N_i} as,

$$\frac{dx}{dt} = -\frac{i_{N_i}}{Q_{\max}} \tag{14}$$

where $Q_{\max}$ is the maximum charge stored in the battery for a given capacity. In addition, the battery terminal voltage can be related to the current, considering internal potential losses, as,

$$v = E_{N_i} + R_i \cdot i_{N_i} \tag{15}$$

where R_i (Ω) is a fitting parameter representing overall internal resistance due to ohmic, surface kinetic and concentration limitation losses.

B. Thermal Process

To simplify, we consider the heat generations due to the enthalpy of reactions [8] and the heat transported by the thermal terminal only, while the heat due to isometric

process, enthalpy of mixing, phase change and change of specific heat are ignored without introducing significant error. The temperature change of the battery is governed by the energy balance equation, as given by,

$$c_p m \frac{dT}{dt} = i_{N_i}\left(v - E_{N_i} + T\frac{\partial E_{N_i}}{\partial T}\right) + i_{O_2}\left(v - E_{O_2} + T\frac{\partial E_{O_2}}{\partial T}\right) + i_T \cdot T \tag{16}$$

where m, the average battery mass (kg), c_p, the average specific heat (J/kg/K), are assumed constant. The first and second term on the right-hand-side are, according to Bernardi et al [8], owing to the enthalpy of reactions, which can be categorized into two processes: $i_{N_i}(v - E_{N_i})$ and $i_{O_2}(v - E_{O_2})$ are polarization heat and irreversible (electrothermal process), while $i_{N_i}T(dE_{N_i}/dT)$ and $i_{O_2}T(dE_{O_2}/dT)$ are entropic heat associated with electrochemical reactions therefore thermodynamically reversible (direct chemical-thermal process). The last term on the right-hand side is the heat transported to (or from) the surroundings through the battery surface, which is modeled as a thermal terminal, with the thermal current i_T as the through variable and the temperature as the across variable. The product of the thermal current and the temperature represents heat power flowing out of the thermal terminal via various heat transfer mechanisms.

C. Pressure Modeling

The pressure of the Ni-H_2 battery is an indicator [3] for the state of discharge or the potential under the condition of regulated charge/discharge. A pressure sensor is usually built inside the battery vessel, so that a V/P control can be implemented to prevent the battery from overcharge. Assuming the ideal gas law applies, the pressure P, and the amount of hydrogen n_{H_2} (in moles) can be specified by the following equations:

$$p = \frac{n_{H_2} RT}{V_g} \tag{17}$$

$$\frac{dn_{H_2}}{dt} = \frac{i_{N_i}}{2F} \tag{18}$$

The initial mole number for the hydrogen is determined by the initial state of discharge according to,

$$n_{H_2}\big|_{t=0} = \frac{3600 C_b}{2F}\left(1 - x\big|_{t=0}\right) \tag{19}$$

where C_b is the battery capacity (in ampere-hour). The partial pressure of oxygen is ignored. Since the rate of reactions is not too fast, any appreciable oxygen produced will be immediately removed via reaction (4).

III. VTB Implementation

The VTB implementation of the model given by (5) to (19) involves 1) defining appropriate terminals for power or signal coupling, and 2) deriving the terminal equations in their standard RC format, and 3) developing C^{++} code for computer execution. The time-domain solution for coupled physics processes of the battery can then be obtained through VTB simulation for any given circuital configurations.

The physical electric terminals of the battery are its anode and cathode for power coupling. Naturally, the current and the potential are defined as the through and across variables respectively. The physical thermal terminal is the battery surface through which the heat can transfer to or from the surroundings. By definition, the thermal terminal can transport heat power by means of conduction, or radiation, or convection. The pressure terminal is a signal terminal, and there is no actual mass or energy flow at this terminal. The definition of the terminals and variables, together with the Ni-H_2 battery icon in VTB schematic view, are shown in Fig. 1.

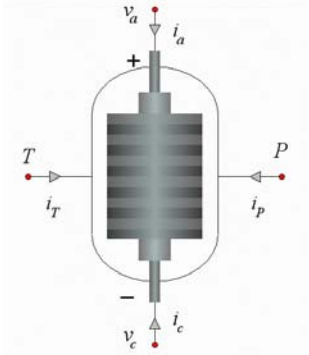

Fig. 1. VTB schematic view of the Ni-H_2 battery. Anode and cathode are the electrical terminals, T the thermal terminal, and P the pressure signal terminal.

Observing that the electrochemical and electrothermal processes are coupled, the terminal through variables are generally functions of all possible terminal across variables. Specifically, we expect that,

$$i_j(t) = \sum_k g_{j,k} k(t) - b_j(t-h), \quad j, k = v_a, v_c, T, P. \tag{20}$$

where h is the simulation time step, $g_{j,k}$ is the admittance of the through variable i at terminal j with respect to the across variable v at terminal k, $b_j(t-h)$ is the time history for the through variable at terminal j, and,

$$g_{j,k} = \left.\frac{\partial i_j}{\partial k}\right|_{t-h}, \; b_j(t-h) = -i_j(t-h) + \sum_k g_{j,k} k(t-h),$$
$$j, k = v_a, v_c, T, P.$$

In above and subsequent equations, j is for subscripts only, but k is used to denote both subscripts and across variables of v_a, v_c, T and P. a and c are used as subscripts for the anode and cathode for simplicity. In matrix notation, equation (20) is of the following form,

$$\mathbf{I}(t) = \mathbf{G}(t-h)\mathbf{V}(t) + \mathbf{B}(t-h), \tag{21}$$

where $\mathbf{I}(t) = \{i_k(t)\}_{4\times1}$, $\mathbf{V}(t) = \{k(t)\}_{4\times1}$, $\mathbf{G}(t-h) = \{g_{j,k}\}_{4\times4}$, and $\mathbf{B}(t-h) = \{b_j(t-h)\}_{4\times1}$, $j, k = v_a, v_c, T, P$.

For the time-discretized vector equation (21) to accurately represent the characteristics of the Ni-H_2 battery, the calculation of the admittance matrix $\mathbf{G}(t\text{-}h)$ and the time history vector $\mathbf{B}(t\text{-}h)$ is critical. In fact, the RC model (21) can yield satisfactory results provided that the simulation time step is sufficiently small.

IV. Static Characteristics

The dynamic model for the nickel hydrogen battery is built based on equation (21) for VTB simulation. Shown in Fig. 2 is a circuit to test the characteristics of the battery. The electrodes are connected to a current load capable of sourcing or sinking current. A heat sink is connected to the thermal terminal to maintain the battery temperature in nearly a constant. The pressure signal terminal is left open at the moment. The battery in Fig. 2 represents a single module with 24 cells in series. Other physical parameter setup is listed in Table 1. The parameters for multi-phase activity are given in Table 2. Also in the simulation, the initial temperature of the battery is set to the ambient temperature, and the initial state of discharge is set to 100%.

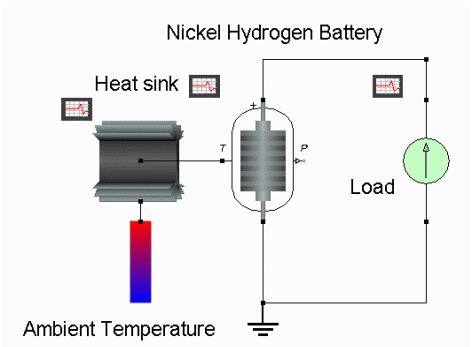

Fig. 2. VTB simulation circuit for the Ni-H_2 battery static characteristics.

Table 1. Parameter Setup for a Single Ni-H_2 Battery Module [10]

Parameter	Value	Unit
Capacity per Module	30	Ah
Gas Volume	$4.65\text{x}10^{-4}$	m^3
Cell Mass	0.05	Kg
Cell Resistance	0.01	Ω
Cell Electrode Area	0.005	m^2
Cell Electrode Thickness	$3.6\text{x}10^{-4}$	m
Specific Heat	1000.0	J/(kg·K)
No. of Cells per Module	24	

Table 2. Parameters for Multi-Phase Activity

$A_0(T)$	$a_0 = 11.50$, $a_1 = -0.0231$
$B_0(T)$	$b_0 = -32.00$, $b_1 = 0.060$
$C(x)$	$c_0 = 4.590$, $c_1 = -15.80$
$D(x)$	$d_0 = 1.800$, $d_1 = -5.680$, $d_2 = 0.350$
$E^0_{Ni}(T)$	$e_{0c} = 1.609$, $e_{0d} = 1.470$, $e_1 = 0.00062$

The simulation was first conducted for a cycle of 16-hour charge at a C/10 rate (0.125 A), 1-hour selfdischarge, and then a discharge at a C/2 rate (0.625 A) till it is depleted. Total runtime is 19 hours. Shown in Fig. 3 is the load current profile. The cycle was repeated for 3 ambient temperatures, 273 K, 283 K and 293 K.

The battery cell voltage are shown in Fig. 4 and compared against the TRW 30 Ah module data [11]. As can be seen, the model fits the experimental data very well for the normal charging (first 10 h) at all three temperatures. The model also has a good agreement with the data for selfdischarge and discharge processes above 1.15 V (16-19 h). During the overcharge processes, the model yields constant overcharge voltages that sharply distinct the normal and overcharge regions, while the experimental data show slow ramps before reaching ultimate overcharge voltage. One of the possible reasons for the discrepancy may be due to strong nonlinear overpotentials resulted from various mechanisms in the overcharge process, which are not included in the model. Notice that voltages at the end of overcharge from the model are very close to those of the experiment, which are about 1.56 V, 1.52 V and 1.47 V respectively for the temperatures of 273 K, 283 K and 293 K. The behaviors of the voltage under the effect of temperatures are consistent with the experimental data over the entire cycle. That is, lower temperatures yield higher voltages and also longer discharge life, suggesting that the battery is preferably operated at low temperature for high-power efficiency. The significant discrepancy between the model and the data is seen when discharging below 1.15 V, where the experimental data show larger discharge capacity due to the appearance of γ-phase of nickel oxyhydroxide [11], and the temperature effect is more pronounced. Although the model does not account for the discharge behavior below 1.15 V, it can be concluded that the model matches the experimental data very well within the normal operation range.

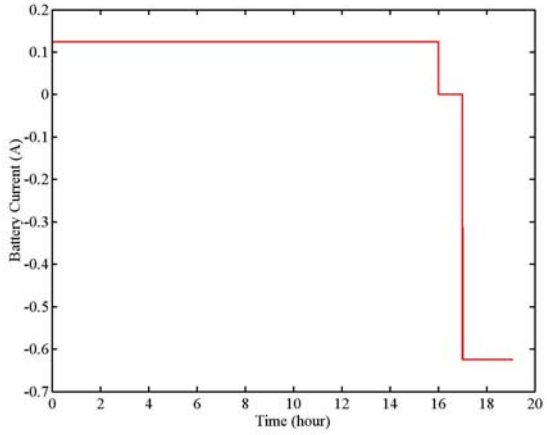

Fig. 3. The current profile for the cycle test of the Ni-H_2 battery.

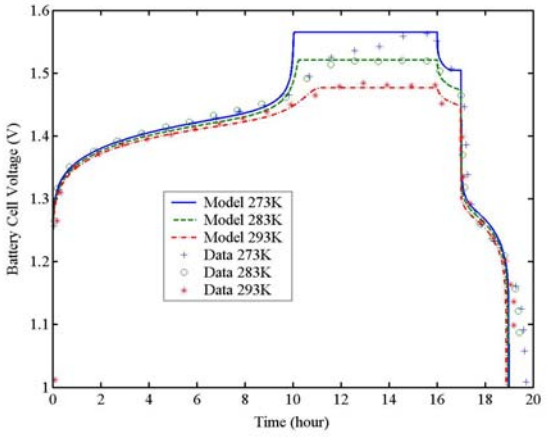

Fig. 4. The cell voltages in a cycle at 3 ambient temperatures.

Fig. 5 and 6 show the nickel reaction current and the oxygen reaction current respectively for the same cycle and for the same 3 ambient temperatures. At any moment, the sum of the nickel current and oxygen current is equal to the total current (Fig. 3). These figures clearly show how a dominant nickel reaction in a normal charge process transits to a dominant oxygen reaction in an overcharge process. During the overcharge process, majority charge current is wasted for oxygen reaction since the energy is not used for oxidizing nickel hydroxide. Significant portion of the current also goes to the oxygen reaction if the temperature is high (see curves for 293 K) even for a normal charge. During the self-discharge process, the reduction of the nickel hydroxide is the only source for a large oxygen reaction current, therefore yielding currents of equal amount but opposite directions from the nickel reaction and the oxygen reaction. During a normal discharge at a C/2 rate, the oxygen current is minimal.

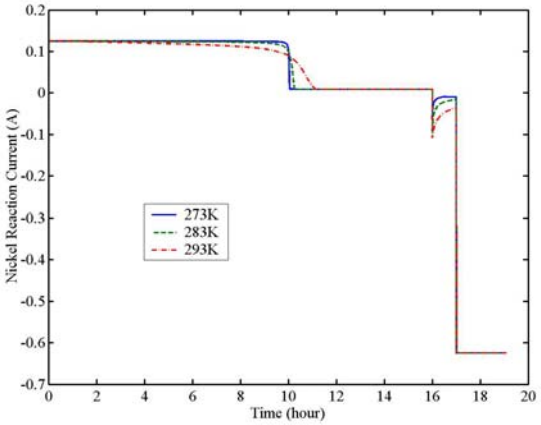

Fig. 5. The nickel reaction current in a cycle at 3 ambient temperatures.

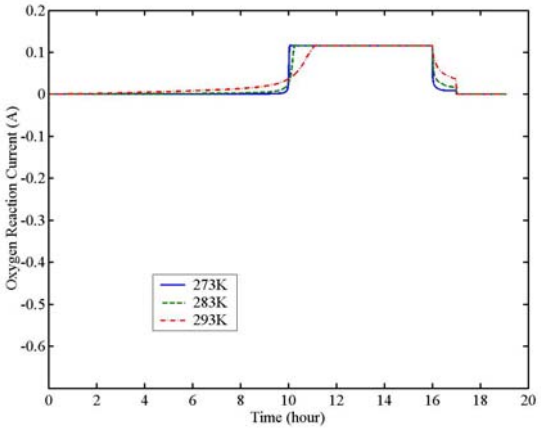

Fig. 6. The oxygen reaction current in a cycle at 3 ambient temperatures.

Fig. 7 shows the state of discharge for the same cycle at the same 3 temperatures. The state of discharge varies almost linearly for a constant charge or discharge rate. For overcharge, it is no longer decreasing but rather maintaining a constant value. The value is higher for a higher temperature, resulting in a lower battery voltage, and a temperature-dependent discharge capacity. Noticeably, the pressure profile shown in Fig. 8 is complementarily similar to the state of discharge. This is in fact due to the amount of hydrogen stored representing the charge state. However, since the pressure is not only proportional to the hydrogen mass, but also to the temperature, the pressure does not accurately represent the state of discharge. This is seen that the pressure is higher for higher temperatures rather than lower to be consistent with the behavior of the state of discharge during almost the entire cycle, except at the transition region of normal charge and overcharge, for which significant loss of the current to oxygen reaction causes the pressure for 293 K to be lower than the pressure for 283 K. It is to be noted that the positions of the overcharge in the state of discharge diagram and the pressure diagram are essentially coincided. Thus, for the purpose of overcharge protection, our pressure modeling, though a simplified one, still serves the purpose.

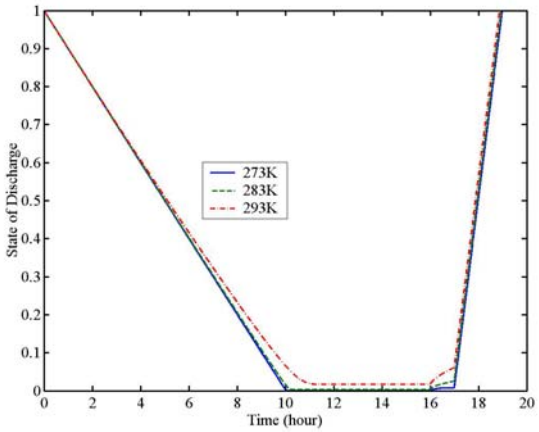

Fig. 7. The state of discharge in a cycle at 3 ambient temperatures.

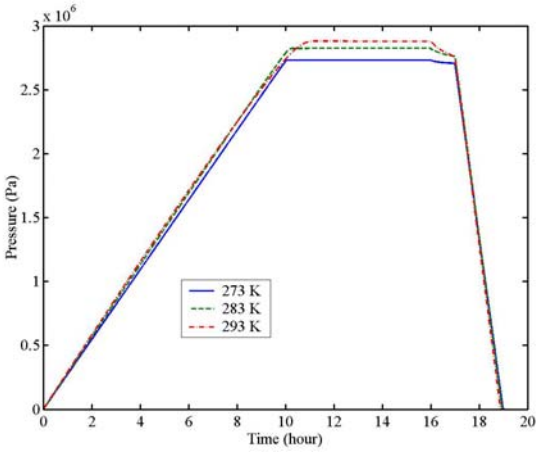

Fig. 8. The battery pressures in a cycle at 3 ambient temperatures.

The temperatures of the battery for the cycle test are recorded in Fig. 9. Notice that the TRW 30 Ah module has an effective heat transfer area of 0.06 m^2. To maintain a constant battery temperature during the test, the cooling coefficient can be as large as 60 W/m^2K [11], which is reasonable for a forced convection cooling. In our

simulation, a radiation-cooling model is used. The rate of heat transfer was set equivalently to 3.6 W/K, so the conditions for cooling are comparable to the experimental data. As can be seen from Fig. 9, the battery cell temperature is nearly constant for each test, but with small variations. Because of a large cooling coefficient and a small cell mass, a thermal equilibrium between the battery and the ambient was quickly reached. This is shown by the fact that the cell temperature reaches a constant value soon after the battery transits from one steady-state mode to another.

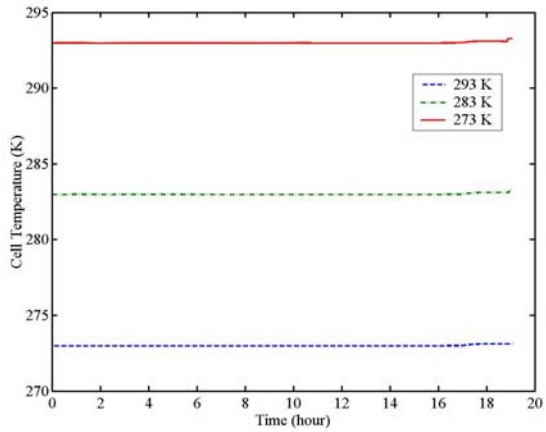

Fig. 9. The Battery cell temperature variations for a cycle at 3 ambient temperatures.

V. Dynamic Simulation

The dynamic behavior of the Ni-H_2 battery is simulated using a simple spacecraft power system as shown in Fig. 10. The spacecraft is a low-orbit satellite of an altitude 798 km, an inclination angle 60° and an orbit about 100 minutes. The shadow time is 35 minutes. The energy source is the solar array (SA), for which a multi-physics model was established [14]. The Ni-H_2 battery array is used for energy storage and supplying power to a load at the shadow time. In order for the battery to operate properly, a constant-current, constant-voltage, pressure-limited control algorithm is employed. The algorithm is implemented by the following components: buck converter (Converter), PID controller (Controller), current sensor (Sensor), and diodes (D1, D2 and D3). Details of these component models can be found in VTB website. Notice that both the battery current and voltage feed back to the controller. In addition, the pressure signal feeds back to the controller for overcharge protection. Thermal radiators to the solar array and the battery are for heat dissipation. For simplicity, a single pulsed power load – transmitter – is used. The parameter setup for the major components is given in Table 3. The solar array are set to deliver power at a high efficiency (no shunt regulator is used), and the battery are set to store and deliver a nearly equal amount of energy in each orbit.

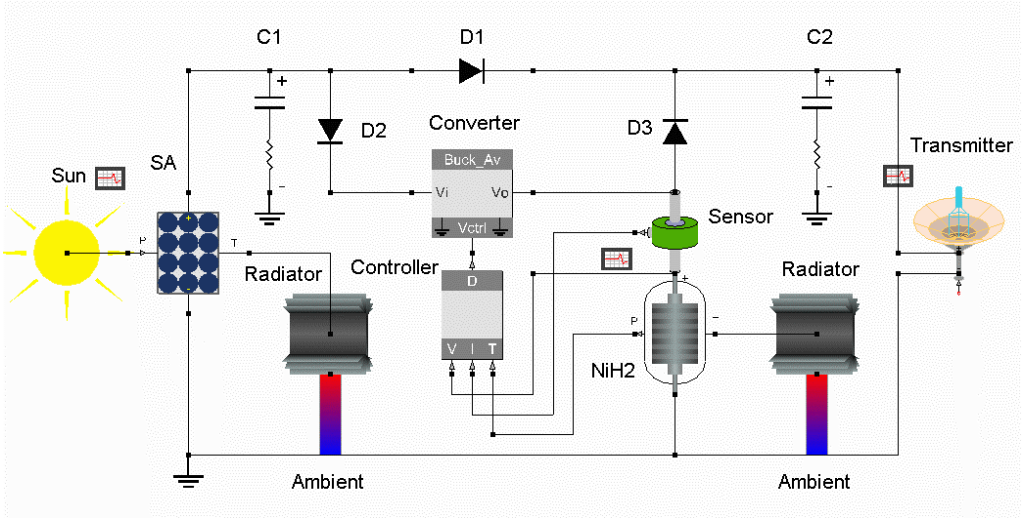

Fig. 10. Spacecraft power system using Ni-H_2 battery as an energy storage device.

Table 3. Parameter Setup for the Spacecraft Power System

Name	Parameter
Spacecraft orbit	Altitude 798 km, inclination 60°, orbit period 100 min., shadow period 35 min.
Solar array	100x30 cells (series by parallel), each cell V_{oc}=0.5 V, active area 0.01 m^2, series resistance 10 mΩ.
Battery array	200 modules in parallel, 24 cells in each module of 30 Ah capacity. Each cell internal resistance 10 mΩ.
Controller	Constant-current charge 32 A, constant-voltage charge 36 V, pressure limit 2.6x10^6 Pa.
Transmitter	3 kW for active duty and 0.25 kW for sleeping period. Duty ratio is 50% for a period of 17.5 min.

The total simulation time is 233.3 minutes, about 2.33 orbits. The results are shown in Figs. 11 to 21. Fig. 11 shows the insolation received by the solar array while it is orbiting. The insolation level is 1357 W/m^2 at the bright side, and zero at the shadow time. The power drawn by the transmitter is shown in Fig. 12. The transmitter is operated at the specified power levels and the cycle rate regardless of insolation levels. Obviously, at the shadow time, the transmitter power is provided by the battery array.

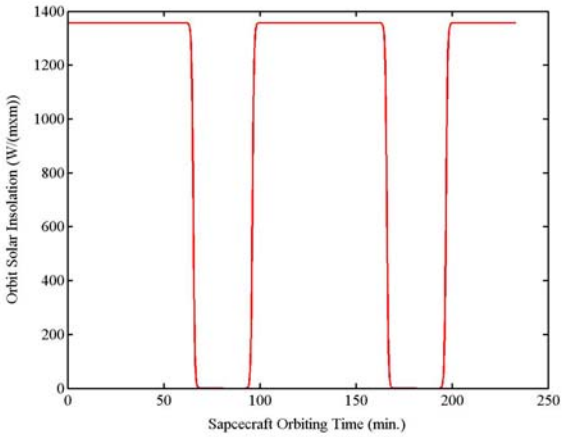

Fig. 11. Solar insolation received by the solar array in the spacecraft as a function of orbiting time.

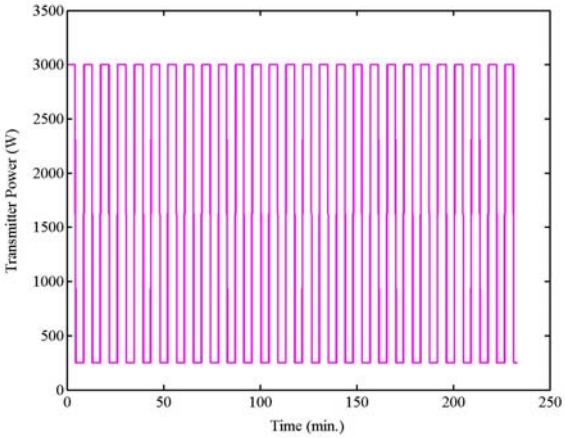

Fig. 12. The transmitter power profile as a function of time. The high power 3 kW, low power 0.25 kW, duty ratio 0.5, and period 17.47 minutes.

Figs. 13 through 16 show the solar array activities (voltage, current, efficiency and temperature) in orbit. When the solar array is illuminated, it converts solar energy and provides electric power to both the transmitter and the battery. Due to a pulsed load, both the array voltage (Fig. 13) and current (Fig. 14) are also pulsating. A high efficiency of 11.5% (Fig. 15) is achieved for a high-power load (3 kW). At a low-power load (0.25 kW), the efficiency is only 3.5%. The energy that is not delivered is then dissipated as heat, thus causing the cell temperature to rise (Fig. 16). When the spacecraft is in the shadow of the earth, the solar array stops converting energy, thus the voltage, current and efficiency are zero, and the cell temperature drops to background temperature. Note that at the time of zero insolation, the voltage does not immediately decay to zero due to the effect of the filter capacitor C1. The spikes of the current waveform at the end and beginning of the shadow periods are due to the transition of the power flow in the system bus. Because the battery voltage (34 V) is lower than that of the solar array (~58 V), we see that the solar array will continue to provide the power to loads at a lower voltage (insolation level is low) during the time of battery transiting from charge to discharge mode, therefore causing a large solar array current. The improvement of system performance, including control of power flow at the transition (the duration that the spacecraft moves from the bright side to the shadow area) is one of our research subjects in the next step.

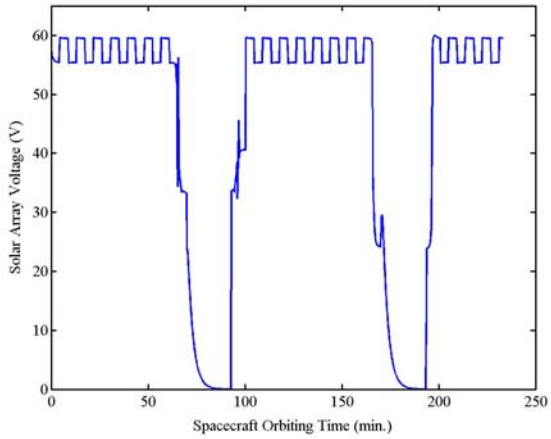

Fig. 13. The solar array output voltage as a function of the time.

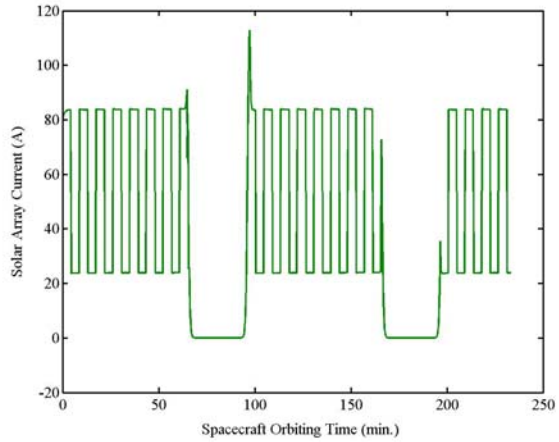

Fig. 14. The solar array output current as a function of orbiting the time.

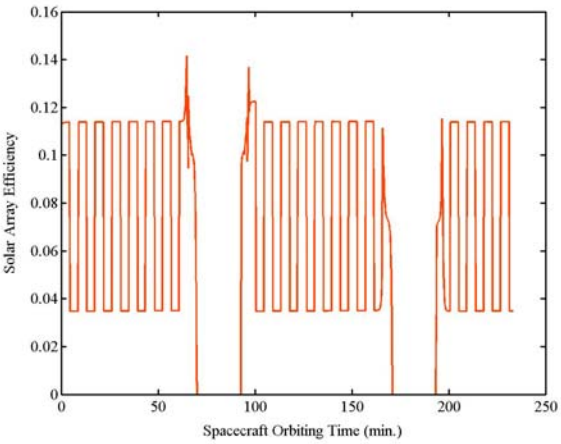

Fig. 15. The energy conversion efficiency of the solar array as a function of the time.

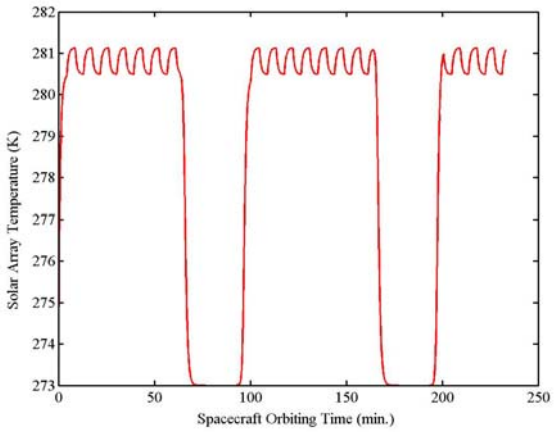

Fig. 16. The solar array cell temperature as a function of the time.

The battery behaviors in orbit are shown in Figs. 17 - 21 (voltage, current, state of discharge, pressure and temperature). When the solar array is illuminated, the battery is charged at a constant current of 32 A (Fig. 18), yielding a charge rate of C/8. The battery voltages (Fig. 17) and pressures (Fig. 20) are increasing, while the state of discharge (Fig. 19) is decreasing. Notice again that the behaviors of the state of discharge and the pressure are complementary. At the shadow period, the battery is on duty to deliver the power to the load at a voltage of ~31 V. Large current ripples are due to a pulsed power load. For a load power of 3 kW (transmitter operating period), the battery current is 130 A, yielding a discharge rate of C/2. For a load power of 0.25 kW (transmitter sleeping period), the current is 20 A, yielding a discharge rate of about C/12.5. Because the total energy stored and delivered in one orbit are nearly equal, the state of discharge restores to its initial value (0.3) at the end of each orbit. This is essentially also true for the pressure. The behavior of the battery temperature is essentially the same as explained previously, small variations due to a forced cooling mechanism.

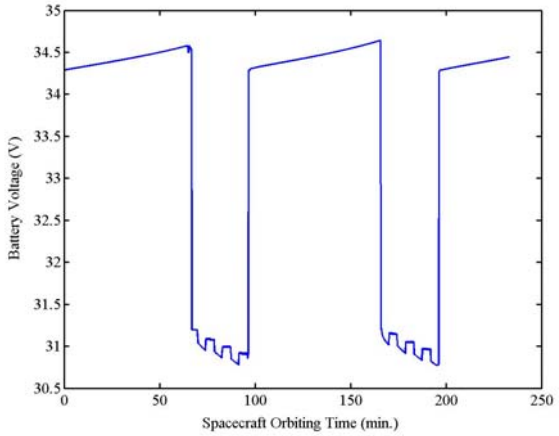

Fig. 17. The battery array voltage as a function of the time.

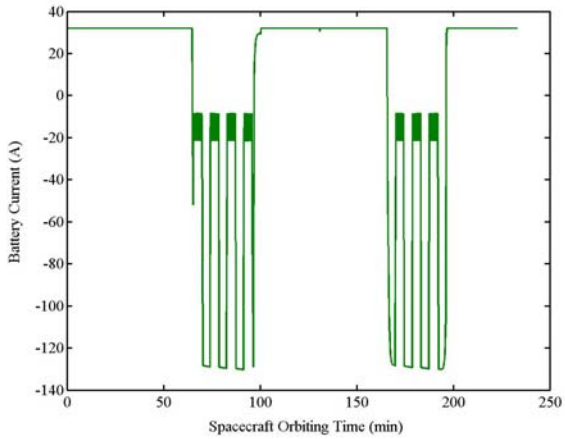

Fig. 18. The battery array current as a function of the time.

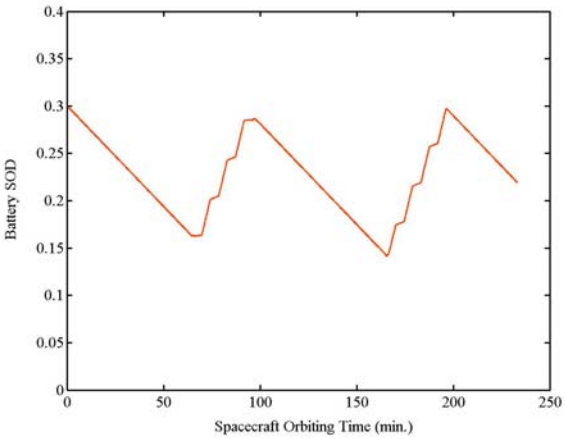

Fig. 19. The state of discharge of the battery as a function of the time.

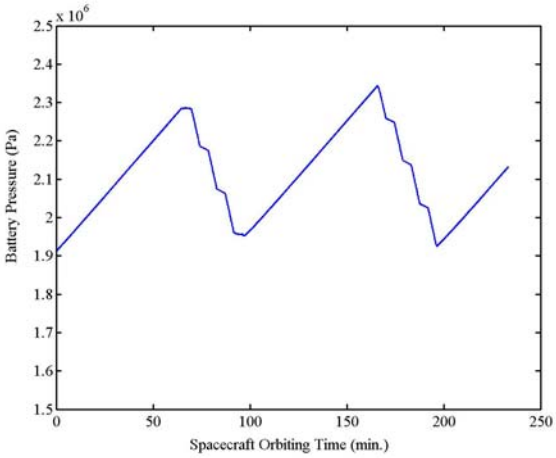

Fig. 20. The battery pressure as a function of the time.

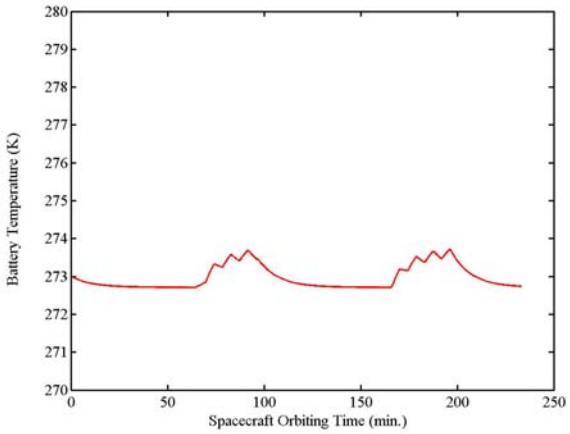

Fig. 21. The battery temperature as a function of the time.

VI. Conclusion

We have established a model in the Virtual Test Bed for the Ni-H_2 battery based on the thermodynamics of one electron redox reaction between nickel hydroxide and nickel oxyhydroxide. The non-ideality of the reversible potential is included by incorporating the multi-phase activity coefficients. The overcharge and the selfdischarge processes are characterized by the oxygen reaction. The details of the energy conversion processes are discussed and the VTB implementation of the model is presented. The model allows for the battery behaviors to be studied in a configurable system while it is dynamically interacting with the system and the environment. The model in general has a good agreement with the experimental results. The dynamic behaviors of the battery in a simple spacecraft electric power system are also demonstrated.

VII. Acknowledgement

This work was sponsored jointly by Veridian MRJ under contract 00-MRJ-1085-100, by the US Army Communications and Electronics Command and the National Reconnaissance Office under contract NRO-00-C-1034.

References

[1] J. D. Dunlop, J. Giner, G. Van Ommering, and J. F. Stockel, *Nickel Hydrogen Cell* (U. S. Patent 3867299, 1975).

[2] J. D. Dunlop, G. M. Rao, and T. Y. Yi, *NASA Handbook for Nickel-Hydrogen Batteries* (NASA Reference Pub. 1314, 1993).

[3] H. Vaidyanathan, H. Wajsgras, and G. M. Rao, Voltage and capacity stability of the Hubble telescope nickel-hydrogen battery, *Journal of Power Sources*, *58*, 1995, 7-14.

[4] P. J. Johnson, S. W. Donley and D. C. Verrier, Orbital simulation life tests of nickel hydrogen batteries with additional non-eclipse cycles, *Journal of Power Sources*, *76*, 1998, 210-214.

[5] S. N. Lvov and D. D. MacDonald, Thermodynamic behavior of Ni-Cd and Ni-H_2 batteries over wide ranges of temperatures (0-200 °C), KOH concentrations (0.1-20 mol kg^{-1}) and H_2 pressure (0.1-500 bar), *Journal of Power Sources*, *72*, 1998, 136-145.

[6] R. A. Dougal, C. W. Brice, R. O. Pettus, G. Cokkinides and A. P. S. Meliopoulos, Virtual prototyping of PCIM systems – the Virtual Test Bed, *Proc. PCIM/HFPC '98 Conf.*, Santa Clara, CA, 1998, 226-234.

[7] M. R. Lightner and S. W. Director, Computer-aided design of electronic circuits, in D. G. Fink and D. Christiansen (Ed.), *Electronics Engineers' Handbook* (New York: McGraw-Hill, 1989).

[8] D. Bernardi, E. Pawlikowski, and J. Newman, A general energy balance for battery systems, *Journal of Electrochemical Society*, *132*(1), 1985, 5-12.

[9] M. Jain, A. L. Elmore, M. A. Mathews and J. W. Weidner, Thermodynamic consideration of the reversible potential for the nickel electrode, *Electrochemica Acta*, *43*(18), 1998, 2649-2660.

[10] B. Wu and R. E. White, Self-discharge model of a nickel-hydrogen Cell, *Journal of Electrochemical Society*, *147*(3), 2000, 902-909.

[11] B. Wu and R. E. White, Modeling of a nickel-hydrogen cell, phase reaction in the nickel active material, *Journal of Electrochemical Society*, *148*(6), 2001, A595-609.

[12] K. P. Ta and J. Newman, Proton intercalation hysteresis in charging and discharging nickel hydroxide electrodes, *Journal of Electrochemical Society*, *146*(8), 1999, 2769-2779.

[13] V. Sinvasan, J. W. Weidner and J. Newman, Hysteresis during cycling of nickel hydroxide active material, *Journal of Electrochemical Society*, *148*(9), 2001, A969-980.

[14] S. Liu and R. Dougal, Dynamic multiphysics model for solar array, *IEEE Trans. Energy Conversion*, *17*(2), 2002, 285-294.